JOURNAL OF GEOPHYSICAL RESEARCH: OCEANS, VOL. 118, 1759–1774, doi:10.1002/jgrc.20155, 2013

A three-dimensional eddy census of a high-resolution global ocean simulation

Mark R. Petersen,[1] Sean J. Williams,[1,2] Mathew E. Maltrud,[1] Matthew W. Hecht,[1] and Bernd Hamann[2]

Received 17 August 2012; revised 6 March 2013; accepted 7 March 2013; published 4 April 2013.

[1] A three-dimensional eddy census data set was obtained from a global ocean simulation with one-tenth degree resolution and a duration of 7 years. The census includes 6.7 million eddies in daily data, which comprise 152,000 eddies tracked over their lifetimes, using a minimum lifetime cutoff of 28 days. Variables of interest include eddy diameter, thickness (vertical extent), minimum and maximum depth, location, rotational direction, lifetime, and translational speed. Distributions of these traits show a predominance of small, thin, short-lived, and slow eddies. Still, a significant number of eddies possess traits at the opposite extreme; thousands of eddies larger than 200 km in diameter appeared in daily data each year. A tracking algorithm found hundreds of eddies with lifetimes longer than 200 days. A third of the eddies are at least 1000 m tall and many penetrate the full depth of the water column. The Antarctic Circumpolar Current contains the thickest and highest density of eddies. Thick eddies are also common in the Gulf Stream, Kuroshio Current, and Agulhas ring pathway. The great majority of eddies extend all the way to the surface, confirming that eddy censuses from surface observations are a good proxy for the full-depth ocean. Correlations between variables show that larger-diameter eddies tend to be thicker and longer lived than small eddies.

Citation: Petersen, M. R., S. J. Williams, M. E. Maltrud, M. W. Hecht, and B. Hamann (2013), A three-dimensional eddy census of a high-resolution global ocean simulation, *J. Geophys. Res. Oceans*, *118*, 1759–1774, doi:10.1002/jgrc.20155.

1. Introduction

[2] How deep are ocean eddies? Do they look more like thin disks or tall columns? Do eddies with large surface extents tend to be deeper as well? How many eddies are completely hidden below the surface? These questions are difficult to answer with current observational data. Detailed eddy characteristics are available from satellite altimetry [*Chelton et al.*, 2011] but provide no information about depth. Shipboard observations provide some hints but are limited to two-dimensional sections and are often shallow in depth [*Timmermans et al.*, 2008; *Nishino et al.*, 2011; *Lilly and Rhines*, 2002]. Ocean floats are an important tool to collect subsurface data and have begun to fill in gaps in recent years but only provide a few profiles for each eddy [*Chaigneau et al.*, 2011].

[3] Numerical simulations of the ocean provide full three-dimensional velocity and tracer fields that lend themselves to automated eddy census and tracking algorithms. A few studies have used regional ocean simulations to investigate eddy characteristics in a particular area. *Doglioli et al.* [2007] tracked the three-dimensional structure of Agulhas rings in an ocean simulation in order to compute transport based on the discrete eddy volume. *Colas et al.* [2011] computed composite vorticity, temperature anomaly, and salinity anomaly structures for cyclones and anticyclones as part of a larger study on transport in the Peru-Chile current system. They show a three-dimensional structure where maximum anomalies occur within the eddies at 100–300 m depth.

[4] *Dong et al.* [2012] developed a three-dimensional eddy data set of the Southern California Bight region (SCB), which provided eddy characteristics at nine vertical levels down to 400 m depth. They find that of the eddies that appear at the surface, less than 20% reach to 50 m, and less than 5% extend to 100 m depth (their Figure 16). Looking from the bottom up, a similar tendency is seen: of the eddies that exist at 400 m, only 15% extend up to 250 m. These data suggest that the great majority of eddies in the SCB are not tall columns but rather thin disks that are vertically isolated, both at the surface and at greater depths. The lifetime and size of eddies did not vary much with depth in that study, and the majority of eddies that extend from the surface to deeper levels are cyclonic.

[5] Eddy surveys conducted with drifters and floats typically provide information about the number of loops observed and the sign of vorticity of these loops, in order to characterize a region's eddy population [*Griffa et al.*, 2008;

Additional supporting information may be found in the online version of this article.

[1]Los Alamos National Laboratory, Los Alamos, New Mexico, USA.
[2]Institute for Data Analysis and Visualization, Department of Computer Science, University of California, Davis, California, USA.

Corresponding author: M. R. Petersen, Los Alamos National Laboratory, MS B296, Los Alamos, NM, 87545, USA. (mpetersen@lanl.gov)

2169-9275/13/10.1002/jgrc.20155

Shoosmith et al., 2005; *Prater*, 2002; *Paillet et al.*, 2002]. However, it is difficult to quantify the horizontal and vertical extents of eddies with these sparse Lagrangian data. Recently, *Chaigneau et al.* [2011] demonstrated a more comprehensive approach by combining Argo float profiles and satellite altimetry data to analyze the vertical and horizontal structures of mesoscale eddies in the eastern South Pacific Ocean. Significant differences were found between cold-core cyclonic eddies and warm-core anticyclonic eddies. Composite averages of nearly 1000 Argo profiles within eddies show that cyclonic eddies are shallower, with an average vertical extent of trapped fluid extending to a depth of 240 m versus 530 m for anticyclonic eddies. The vertical structure of temperature, salinity, and density anomalies are detailed for these composite eddies, which allows the authors to compute heat, salt, and volume transport due to eddies. Similarly, *Souza et al.* [2011a] combined float and satellite data to estimate heat fluxes and transport by Agulhas rings.

[6] The characterization of ocean eddies is the first step towards understanding their effects in the transport of heat, salt, chemical species, and organisms. The time variability of ocean currents is several times larger than the mean flow, as measured by eddy kinetic energy versus mean kinetic energy in drifter observations and high-resolution global models [*Thoppil et al.*, 2011]. Despite the name, eddy kinetic energy is a measure of any time-varying part of the velocity field, including discrete eddies as well as meandering jets and waves. Discrete eddies have been shown to play a major role in observed heat and salt transport [*Roemmich and Gilson*, 2001; *Chaigneau et al.*, 2011] and water mass and momentum transport in model studies [*Doglioli et al.*, 2007]. Discrete eddies account for 60% of the eddy kinetic energy in strongly eddying currents such as the Antarctic Circumpolar Current (ACC) and western boundary currents [*Chelton et al.*, 2011].

[7] Observational studies have shown that discrete eddies can have a large impact on biological productivity [*Everett et al.*, 2011; *Benitez-Nelson et al.*, 2007]. *Nishino et al.* [2011] measured increased ammonia concentrations in a warm-core eddy that originated on the shelf and moved to the Canada Basin. They suggest that the eddy was responsible for sustaining 30% higher concentration of picophytoplankton biomass than that of the surrounding waters. *Falkowski et al.* [1991] reported an increase in total primary production of 20% due to eddy pumping in the tropical Pacific. Eddy-driven slumping of the basin-scale north-south density gradient has been observed to cause a springtime phytoplankton bloom 20–30 days earlier than would occur by warming alone [*Mahadevan et al.*, 2012].

[8] How deep do the effects of eddies extend? *Adams et al.* [2011] found correlations between surface and deep velocities of mesoscale eddies in observations and model studies of the northern East Pacific Rise. These deep-reaching eddies transport hydrothermal vent efflux and vent larvae away from the rise and provide a mechanism for dispersing propagules (plant spores) hundreds of kilometers between isolated and ephemeral communities. Acoustic measurements show that anticyclonic eddies shape the distribution and density of marine life from the surface to depths of hundreds of meters [*Godø et al.*, 2012].

[9] The purpose of this paper is to characterize eddies of the global ocean, in particular properties involving depth that are somewhat sparse in observational studies. To our knowledge, this is the first such eddy census of a global ocean simulation. Past work on vertical eddy structure is limited to regional domains on continental shelves [*Doglioli et al.*, 2007; *Colas et al.*, 2011; *Dong et al.*, 2012]. The paper is organized as follows: we first describe the ocean model and numerical simulation (section 2) and eddy identification method (section 3), followed by a description of eddy characteristics (section 4) and conclusions.

2. Numerical Simulation

[10] The eddy census was conducted using velocity data from 7 years of a longer simulation of POP (Parallel Ocean Program, http://climate.lanl.gov/Models), developed and maintained at Los Alamos National Laboratory [*Smith et al.*, 1992]. POP is the ocean component of the Community Earth System Model (CESM, cosponsored by the Department of Energy and the National Science Foundation), which is used to study past, present, and future climate [*Meehl et al.*, 2006]. CESM simulations provide data for the Intergovernmental Panel on Climate Change (IPCC) Working Group I publications on "The Physical Science Basis" for climate change [*IPCC*, 2007].

[11] POP is a publicly available, z-level, hydrostatic, Boussinesq primitive equation ocean model that allows for generalized orthogonal horizontal grids. In order to simulate an actively eddying ocean, the particular configuration used for this study has horizontal resolution of 1/10° at the equator. The Southern Hemisphere is a standard Mercator grid, while the Northern Hemisphere has two poles to avoid singularity and to provide more uniform grid spacing in the Arctic, resulting in grid cell spacing ranging from 3 km at high latitudes to 11 km at the equator. The model contains 42 fixed vertical levels ranging in thickness from 10 m at the surface to 250 m at depth, with partial bottom cells [*Adcroft et al.*, 1997] employed to provide a more accurate depiction of the bathymetry. Other features include an implicit free surface [*Dukowicz and Smith*, 1994], vertical diffusion using K-Profine Parameterization (KPP) [*Large et al.*, 1994], and biharmonic momentum and tracer diffusion. The ocean is forced by monthly surface wind stress, heat fluxes, and fresh water fluxes calculated from the "normal year" of the Coordinated Ocean-Ice Reference Experiment (CORE) data set [*Griffies et al.*, 2009] and has no explicit sea ice model. Further details and references can be found in *Maltrud et al.* [2010].

3. The R^2 Method of Eddy Identification

3.1. Motivation

[12] A number of methods are available to identify eddies: sea surface height anomalies above a particular threshold [*Fang and Morrow*, 2003; *Chaigneau and Pizarro*, 2005]; the value of the Okubo-Weiss parameter based on velocity fields [*Isern-Fontanet et al.*, 2003]; and more sophisticated algorithms that combine these with a set of additional criteria [*Chelton et al.*, 2011]. Other methods search for reversals in velocity sign [*Nencioli et al.*, 2010] or for streamlines with circular or closed geometry, like the

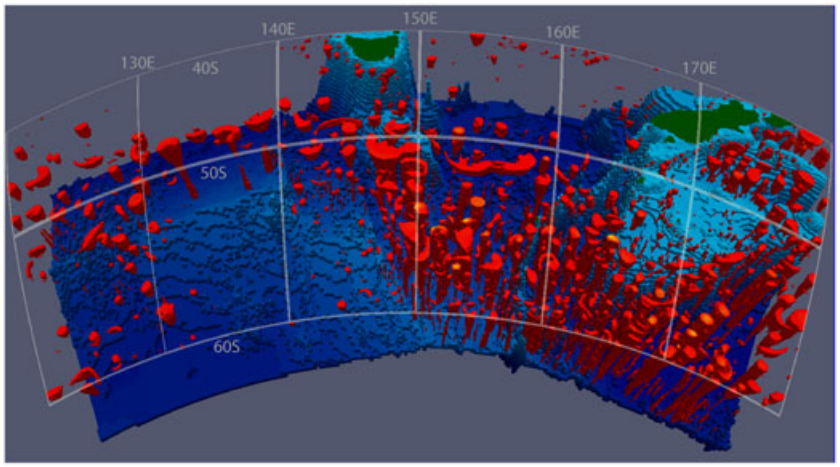

Figure 1. Okubo-Weiss field in the Southern Ocean to the south of Tasmania and New Zealand, showing 120°E–180°E and 45°S–55°S and an isosurface of $W/\sigma_W = -0.2$. The Antarctic Circumpolar Current is the region with the largest number of eddies and the deepest eddies in the world. Many of these eddies extend to the full depth of the ocean; others are strictly surface features, and some are completely submerged. The R^2 method is more discriminating and will eliminate many of the more spurious features seen here. Depth is exaggerated by a factor of 50.

curvature center method [*de Leeuw and Post*, 1994] and the winding-angle method [*Sadarjoen and Post*, 2000].

[13] The most widely used methods are based on the Okubo-Weiss (OW) parameter W, a measure of strain versus vorticity [*Isern-Fontanet et al.*, 2006]:

$$W = S^2 - \omega^2 \quad (1)$$

$$= s_n^2 + s_s^2 - \omega^2 \quad (2)$$

where $\omega = u_{2,1} - u_{1,2}$ is the vertical component of the relative vorticity, and S, the horizontal strain, is composed of a normal component $s_n = u_{1,1} - u_{2,2}$ and a shear component $s_s = u_{1,2} + u_{2,1}$. Here $u_{i,j}$ are the components of the velocity gradient tensor. Ideally, OW contours can be used to identify vortices because OW is negative in the inner vortex core, where the flow is vorticity-dominated, positive in the strain cells surrounding the core, and small in magnitude for the remaining background flow (Figure 1). This is certainly true for idealized, periodic flows [*Petersen et al.*, 2006], but in global ocean simulations with boundaries and realistic forcing, there are also large negative OW values along meanders of strong currents and land boundaries (Figure 2a).

[14] A threshold of $W/\sigma_W \leq -0.2$ is typically chosen to identify the eddy edge [*Isern-Fontanet et al.*, 2006; *Henson and Thomas*, 2008; *Xiu et al.*, 2010; *Petersen et al.*, 2006]. Here σ_W is the standard deviation of W over the region of interest, e.g., the global ocean domain in this study. However, eddy identification is sensitive to the value of σ_W and the threshold chosen. Because σ_W varies substantially over different regions of the ocean, it is not clear how to choose this value over the whole globe for this study.

[15] For these reasons, we decided to perform our global eddy census based on the R^2 method presented in *Williams et al.* [2011b], which judges the fitness of a vortex based on similarity of characteristics with an idealized Gaussian vortex. Such a vortex has a Gaussian vorticity distribution in the radial direction and has been used as a model for oceanic eddies in both analytic and observational studies [*Dewar and Killworth*, 1995; *Riser et al.*, 1986].

3.2. The R^2 Method

[16] The R^2 method is as follows. For each vortex identified in a W field, the algorithm begins at the minimum W value and computes the area (or volume) added with small increments of W. For a Gaussian vortex, this relationship is nearly linear in the vortex core and then drops off dramatically at the vortex edge. Thus, a simple linear regression may be used to judge how well an eddy conforms to this characteristic of a Gaussian vortex. For each vortex, at each increment of W, one computes the measure of the coefficient of determination,

$$R^2 = 1 - \frac{\sum_{i=1}^{N}(a_i - f_i)^2}{\sum_{i=1}^{N}(a_i - \bar{a})^2} \quad (3)$$

where a_i is the area encompassed by the W contour, $f = C_1 + C_2 W$ is the best-fit line to area versus W, f_i is the value of that function for a particular W_i, $\bar{a} = \sum_{i=1}^{N} a_i/N$, and i increments through increasing values of W. The R^2 value describes how well a line fits the relationship between $a_1 \ldots a_N$ and $W_1 \ldots W_n$.; a value of 1 indicates a perfect linear fit. In the R^2 method, a confidence threshold is chosen for the full domain. For well-formed eddies, the R^2 value is above 95% within the eddy core and then drops off outside the eddy as the area versus W fit becomes poor. For eddies that are less Gaussian-like, the R^2 value may only reach 75% or 80%. Thus, in the R^2 method, one chooses a confidence threshold of the fit to a Gaussian vortex rather than a particular OW threshold or normalization.

[17] In our problem of the characterization of eddies in oceanic flow, the extension of the R^2 method to the third dimension is straightforward, as the area in (3) may be replaced with volume, and the rest of the algorithm remains the same. OW is computed for the full three-dimensional (3-D) horizontal velocity field, i.e., at every model level. The

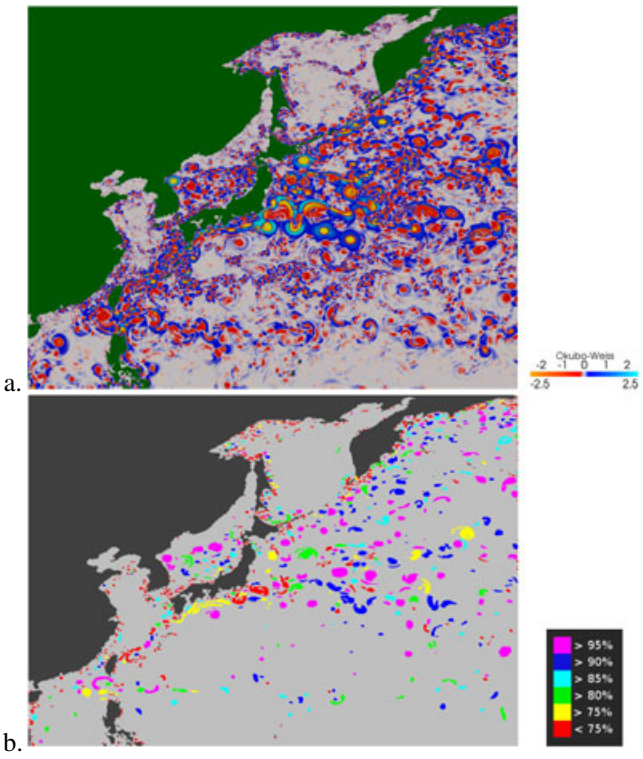

Figure 2. (a) Okubo-Weiss values over a region including the Kuroshio Current. With a standard OW method, all the red areas would be identified as candidate vortices. (b) Using the R^2 method, each high-vorticity feature has a confidence threshold associated with it. Features with a confidence threshold > 95% (magenta) are well-formed vortices, while those with a confidence threshold < 75% (red) are small, noisy features, mostly found near land boundaries. Those in between are a mix of sheared and deformed vortices. A 90% confidence threshold is used for the remainder of this study.

OW computation uses horizontal velocities only, as they are several orders of magnitude larger than vertical velocities in oceanic flows. The boundary of a 3-D eddy is defined by an isosurface of OW. This OW value may be different for each eddy and is computed as the value when the linear fit of OW versus volume within that OW isosurface drops below the confidence threshold. The identification of grid cells within an eddy does not depend on the choice of OW normalization (usually the standard deviation) and could be performed on an unnormalized OW field.

[18] To see the extension from 2-D to 3-D with horizontal velocities, we review the description of the R^2 method for a 2-D Gaussian vortex presented in *Williams et al.* [2011b, section 3] and continue to a general formulation for a 3-D ocean eddy. A 2-D idealized Gaussian vortex [*Kundu et al.*, 2012, section 3.5] located at $\tilde{\mathbf{x}}$ may be described by its vorticity as a function of r, the radial direction, as

$$\omega(x,y) = c_1 \exp\left(\frac{-|\mathbf{x}-\tilde{\mathbf{x}}|^2}{2c_2^2}\right), \tag{4}$$

where $\mathbf{x} = (x,y)$, c_1 and c_2 are parameters that control the maximum strength and the width of the vortex, respectively. The extension of this idealized vortex to 3-D is

$$\omega(x,y,z) = c_1(z) \exp\left(\frac{-|\mathbf{x}_{2D}-\tilde{\mathbf{x}}_{2D}(z)|^2}{2c_2^2(z)}\right), \tag{5}$$

where ω is the vertical component of the relative vorticity. The strength c_1, width c_2, and vortex center $\tilde{\mathbf{x}}_{2D}$ may now vary in the vertical, and $\mathbf{x}_{2D} = (x,y)$. These three parameters allow the idealized vortex to take on shapes such as a column, vase, or bulb, as well as include tilting or spiraling. The only constraint is that variations in $\tilde{\mathbf{x}}_{2D}$ are sufficiently small so that this remains a coherent vortex in the vertical, i.e., gridcells within a particular *OW* isosurface remain a connected set. For a rotating, stratified fluid like the ocean, vertical velocities are much smaller than horizontal velocities, so this idealized vortex only considers the vertical component of vorticity. From these formulas for idealized Gaussian vortices, we may compute plots of OW versus volume and OW versus R^2, as shown in *Williams et al.* [2011b, Figure 4] for 2-D; 3-D cases produce similar curves. For more complex 3-D vortices, it is best to evaluate the method on realistic eddies extracted from high-resolution ocean model output. Many individual eddies were tested in the development of the R^2 method; for example, the R^2 linear fit is very good for a well-shaped Agulhas eddy but poor for a deformed meander [*Williams et al.*, 2011b, Figure 7]. There is no pre-imposed vertical structure used in the eddy detection algorithm. Rather, the 3-D structure comes directly from an isosurface in the 3-D Okubo-Weiss field.

[19] The R^2 algorithm is described as follows [*Williams*, 2012]. After loading velocity fields, the OW field is computed for the full domain on a single day. Each local minimum in OW is a potential seed point for an eddy. The volume and OW value of the seed gridcell are the first entry in a record of cumulative volume and increasing OW values. From the seed point, the six possible nearest neighbors (specifically, those grid cells that share a face with the seed cell) are evaluated, and the one with minimum OW adds a new entry to the cumulative volume-OW record. The algorithm proceeds by tracking "eddy cells" and "neighbor cells" of this eddy. At each iteration, the neighbor cell with the minimum OW value is converted from a neighbor cell to an eddy cell. The linear fit of volume versus OW is evaluated after the addition of each new eddy cell but only after a minimum OW value is passed, typically –0.5. If the coefficient of determination (3) is less than the confidence threshold at that point, the eddy is not counted. Otherwise, the algorithm proceeds until the coefficient of determination falls below the confidence threshold, and that value of OW determines the eddy boundary (i.e., all cells recorded as "eddy cells" at that point are within the eddy boundary). Census information such as location, size, depth, etc., are then added to the database for that eddy. Because multiple local OW minima may exist in a single eddy, the algorithm checks for duplicate eddies as it proceeds. Note that this algorithm treats horizontal and vertical neighbors in the same way.

[20] In order to make the R^2 algorithm more accessible to the wider community, we have written a well-documented Matlab version with sample data sets, included in the supporting information for this article. Small subdomains of the North Atlantic, Kuroshio, and Agulhas regions have been extracted from a single daily data file of

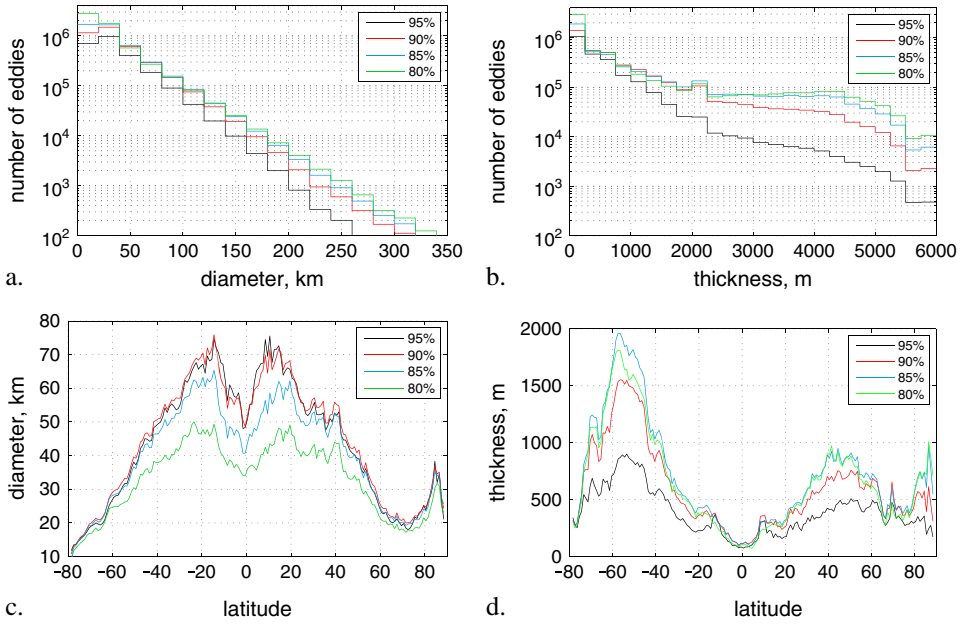

Figure 3. Sensitivity analysis where the confidence threshold of the R^2 method has been varied between 80 and 95%, showing a distribution of (a) eddy diameter; (b) thickness; (c) mean diameter versus latitude; and (d) mean thickness versus latitude. As the confidence threshold is increased, the algorithm becomes more selective in accepting eddies. The majority of eddies removed are less than 20 km in diameter, making mean diameters larger. Both thin and thick eddies are removed as the confidence threshold increases, so that mean eddy thickness is a maximum at the 85% confidence threshold. The sensitivity analysis was conducted on 1 year's daily data, with no minimum eddy lifetime.

horizontal velocity, in NetCDF format. The user may specify the confidence threshold and minimum OW value for the R^2 algorithm. The code produces the eddy census data and plots of velocity fields, OW, eddies identified by OW, and eddies identified by the R^2 method. This example code was written for clarity rather than efficiency and may be speed or memory-limited for larger data sets. Efficiency notes within the code point out how to make the code faster and less memory intensive.

3.3. Tracking Algorithm

[21] In addition to using the R^2 method for detecting eddies, a tracking algorithm was employed to provide data on eddy propagation speed and lifetime. At each consecutive time sample, the algorithm searches for an eddy of similar size at the expected location based on the previous eddy translation velocity. For the analysis presented here, an eddy is considered the same if it appears within $1.5r$ of the expected location, where r is the radius of the larger eddy, and if the radii match within 70%. The radius is the equivalent radius computed from the horizontal area at the depth of the eddy's minimum OW value. These parameters were adjusted so that eddy tracks with smooth trajectories were long and unbroken but were found to be stringent enough that unlikely tracks with abrupt changes in direction were not included. See *Williams et al.* [2011b] and *Williams* [2012] for further details. Most of the results presented in this eddy census use a minimum lifetime of 4 weeks in order to analyze eddies that could significantly influence nonlocal transport in the global ocean.

4. Results

[22] Daily averaged velocity fields were archived from a 7 year run that was restarted from year 75 of the simulation described in *Maltrud et al.* [2010]. The census program identified eddies from each daily average and the eddy tracking algorithm was employed to collect statistics over the lifetime of each eddy. Because an eddy's characteristics change over its lifetime, the statistics shown in the figures include an individual data entry for each eddy on each day it was observed (similar to *Dong et al.* [2012]).

4.1. Eddy Location, Lifetime, and Speed

[23] A total of 10.9 million eddies per year (30,000 per day) were identified in these daily fields using the Okubo-Weiss method with a threshold of $W/\sigma_W = -0.2$, where σ_W is the standard deviation over the surface of the global domain on the initial day. Using the R^2 method with 90% confidence threshold reduces this by almost a factor of 3 to 3.9 million per year (10,700 per day), where most of the removed eddies are small and thin. In addition, the tracking program (which followed over 152,000 eddies over 7 years) was used to remove all eddies with a lifetime of less than 28 days (4 weeks), reducing the count to 0.96 million eddies per year (2600 per day) or about 11 times fewer than Okubo-Weiss alone.

[24] Not surprisingly, the number of eddies detected by the R^2 method is sensitive to the confidence threshold chosen for the Gaussian fit. Considering a single year of model output, the number of accepted eddies decreases from 5.8 million at 80% to 2.4 million at 95%. The majority of the rejected eddies are small, with a diameter of less than 20 km

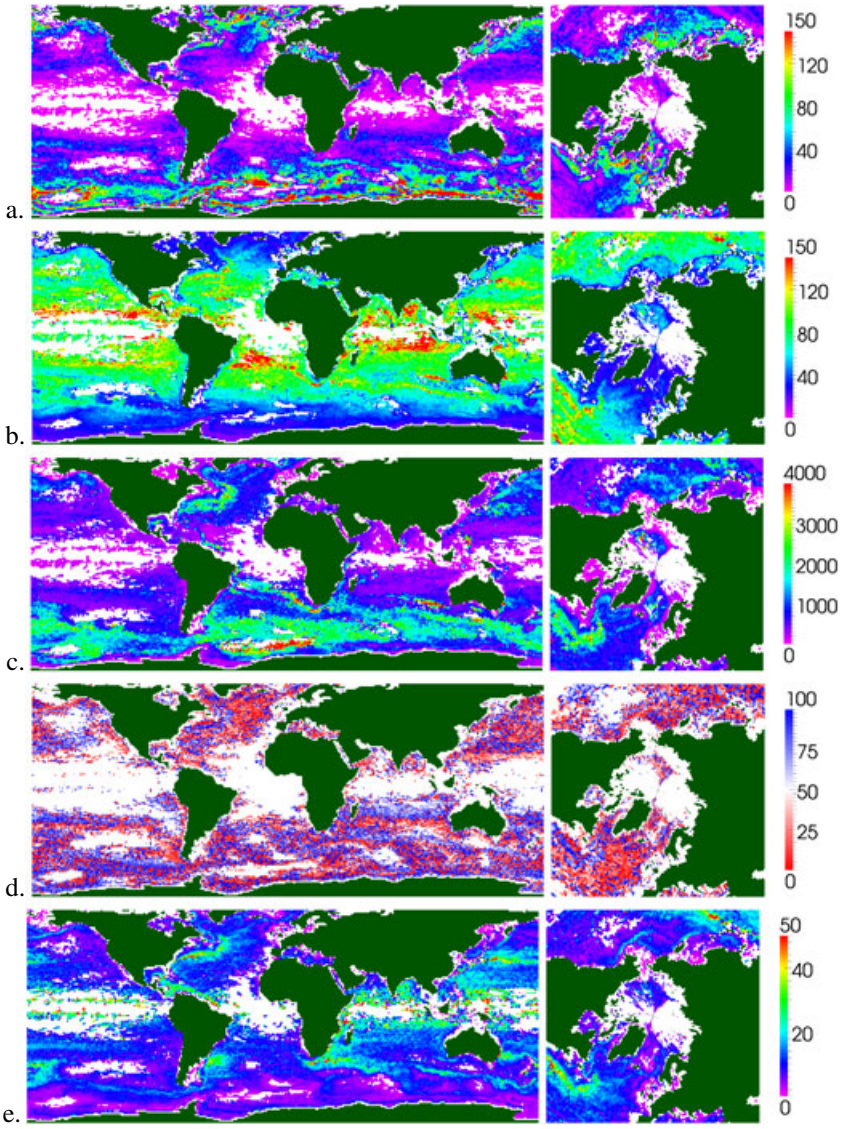

Figure 4. Eddy statistics from 7 years of a POP ocean simulation using the R^2 eddy detection method, a minimum lifetime of 4 weeks, and collated in 1° bins: (a) daily eddy count, where color scale is eddies per year; (b) diameter, km; (c) thickness, m; (d) percent cyclonic; and (e) eddy propagation speed, cm/s. White areas are 1° cells where no eddies were detected over the 7 year census.

(Figure 3a), which increases the mean diameter as the confidence threshold changes from 80% to 90% (Figure 3c). A large number of thin eddies (less than 250 m thick) are removed as the confidence threshold is raised, but thick eddies are removed as well, particularly as the confidence threshold is increased from 90% to 95% (Figure 3b). The mean thickness decreases by about a factor of 2 at most latitudes as the confidence interval increases from 80% to 95% (Figure 3d). As a result of this sensitivity test, it was decided that a 90% confidence interval would be appropriate for this study, although it is unlikely that any conclusions reached would be qualitatively different if a more stringent threshold was used.

[25] A detailed view of the eddy density can be seen by binning daily eddy locations in each 1° grid cell across the globe (Figures 4a and 5b). In order to assess the fidelity of the model eddy count, comparisons can be made with the altimetry-derived census of *Chelton et al.* [2011]. However, such a comparison must be attempted carefully since not only are the sampling methods different (three-dimensional R^2 versus sea surface height criterion), so are the fields that they are sampling (model versus data). In addition, this 7 year study includes eddies with a minimum 4 week lifetime and counts the number of times an eddy occurred in daily data in each 1° square, per year, while *Chelton et al.* [2011] has a minimum 16 week lifetime and counts the number of eddy centroids that pass through each 1° square over a 16 year period. With these differences in mind, we will emphasize the geographical distribution of eddy occurrence rather than magnitudes (Figure 5).

[26] The clearest differences between the model and data are the somewhat larger meridional extent of regions where no eddies are found in the model in the tropical Pacific and eastern tropical Atlantic, as well as the very large number of

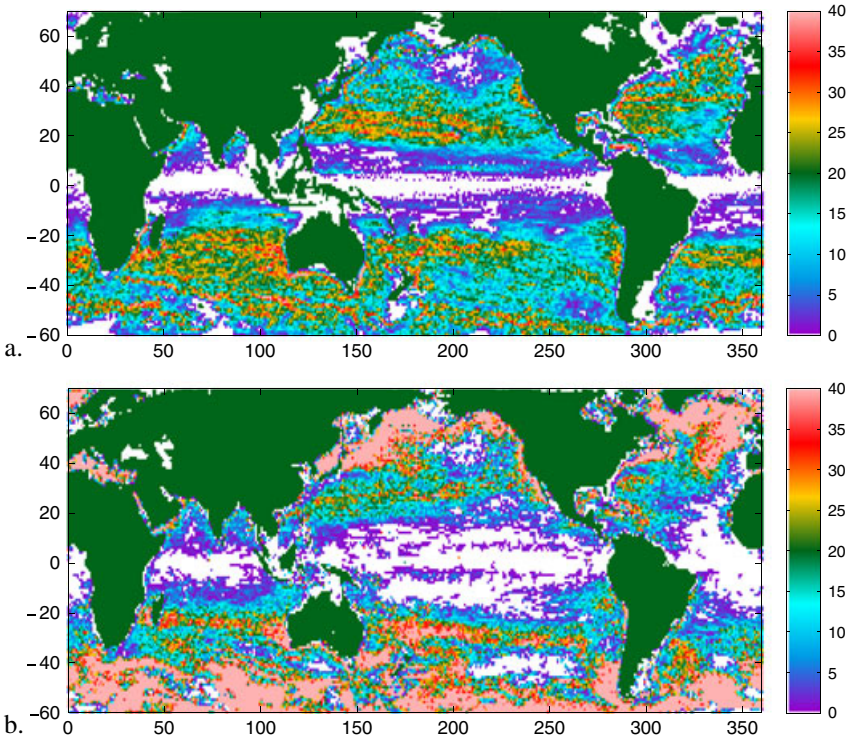

Figure 5. Number of eddies per 1° square from (a) satellite observations of *Chelton et al.* [2011] and (b) this study. Color bar extents were chosen to compare geographical distribution rather than magnitude, as there are several differences between data sets (see text). Overall, observations show a higher eddy density in zonal midbasin bands, while the simulations produce more eddies in western boundary currents and the ACC.

eddies found at high latitudes in the model. The former is consistent with unrealistically low model sea surface height (SSH) variability in the tropics (not shown). The latter is likely due to a number of factors. For example, the model has no explicit sea ice model, which allows sampling of eddies year-round at high latitudes. Increasing the minimum lifetime from 4 to 16 weeks substantially reduces the number of high-latitude eddies (not shown), but this bias remains a question for further study.

[27] There is also an encouraging amount of agreement to be seen in Figure 5. Regions of low eddy density in the North Pacific and the eastern South Pacific have been called "eddy deserts" [*Chelton et al.*, 2011] and are clearly visible in both the data and model. Subtropical zonal bands with high eddy counts can be seen in all basins. In the model, these bands are more sharply peaked as the eddies tend to follow similar paths from year to year. This is possibly due to the fact that the model is forced with repeating monthly climatology and that the wind stress calculation does not include the contribution from the surface ocean velocity. Similarities can also be seen in the eastern basin upwelling zones off the west coasts of Australia, Peru, and the United States.

[28] It is interesting to note that the eddy count in the central and eastern Arctic is extremely sparse (Figure 4a). Unfortunately, very few long-term observations are available (e.g., [*Timmermans et al.*, 2008]) in the high Arctic, so it is difficult to draw conclusions about the fidelity of the simulation there. It is likely that a combination of factors may be causing this, such as insufficient grid resolution, strong restoring of surface temperature and salinity (30 day time scale) to climatological values under prescribed sea ice, or unrealistic model density structure. An eddy census of higher fidelity simulations of the Arctic with dynamic sea ice and higher resolution, like those in *Maslowski et al.* [2008], may shed light on this question.

[29] Collecting eddies into 1° latitude bins allows for a quantitative comparison of the R^2 method and Okubo-Weiss. The R^2 method reduces the eddy count quite uniformly at midlatitudes to high latitudes (Figure 6a) but culls somewhat more strongly in the tropics, where the eddies that are removed tend to be thin and small (Figures 6b and 6c).

[30] Figure 7a shows a histogram of lifetimes for all eddies identified over the 7 year period. As noted above, 75% of eddies identified in daily averages have lifetimes of less than 28 days and were discarded from the analysis since such short-lived eddies are typically not coherent structures involved in nonlocal transport. The longest-lived eddy existed for a duration of 1143 days, nearly half the span of the full data set. This eddy remains nearly still and isolated in the Gulf of St. Lawrence (green track in Figure 8) with a mean thickness of 419 m and mean diameter of 69 km. Other eddies with lifetimes greater than 550 days include three off the coast of Chile, two in the ACC, and one in the northwest Pacific.

[31] An image of the 5000 longest-lived eddies (Figure 8) shows an abundance of eddies in the ACC; these tracks

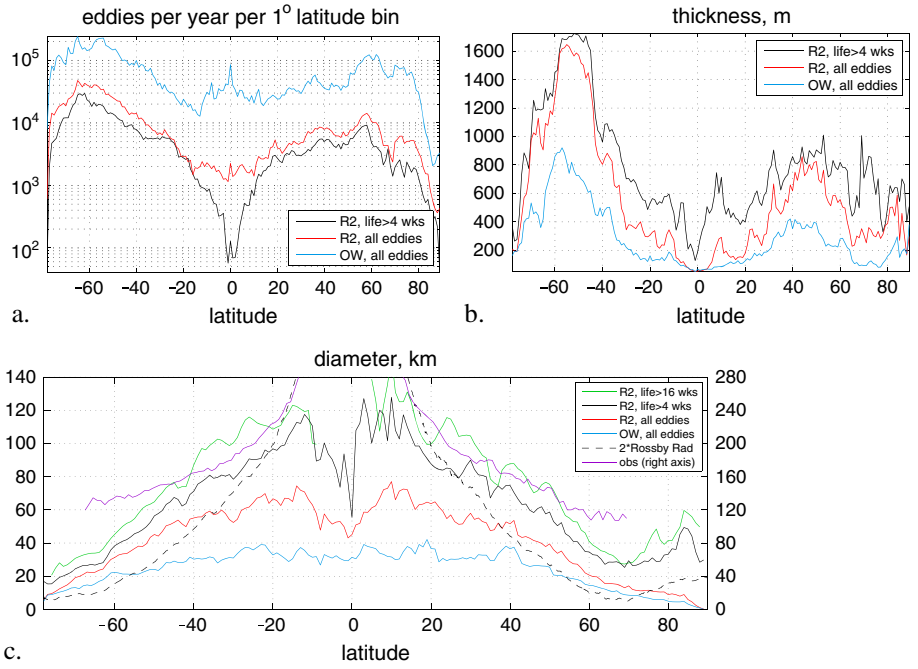

Figure 6. Eddy statistics collected over a 7 year ocean simulation in 1° latitude bins: (a) daily eddy count, (b) thickness, and (c) diameter, showing the Okubo-Weiss method (blue), the R^2 method (red), and the R^2 method with a minimum lifetime of 4 weeks (black) and 16 weeks (green, in Figure 6c only). The black dashed line in Figure 6c is 2 times the first baroclinic Rossby Radius computed using the time-averaged model density field employing the method described in section 2a of *Smith et al.* [2000]. Note that this curve is almost identical to that produced from the model's data-derived initial condition. The purple line in Figure 6c shows the zonally averaged speed-based radius scale from *Chelton et al.* [2011] (note that scale is on the right axis). The R^2 method is more selective than Okubo-Weiss alone, and the lifetime filter further reduces the number, particularly near the equator. Eddies rejected by the R^2 method tend to be small and thin, so that the average eddy diameter and thickness increase. Eddy numbers are counted from each daily entry of the census data.

appear relatively short and chaotic and propagate in all directions. In contrast, the midlatitude eddy tracks are smoother, longer, and predominantly westward. Several tracks have a looping behavior, such as two brown tracks in the mid-North Atlantic. The tracked Agulhas Rings are particularly long and stable and are visible all the way to South America. Because this eddy tracking routine requires similar radii to match from frame to frame, an event that changes eddy characteristics, like merger or shearing in a jet, will sometimes split what appears to be a single track.

[32] The tracking algorithm measures the speed of eddy propagation by computing the distance traveled from 1 day to the next (Figure 7b). The distribution follows a logarithmic dropoff, with 72% of eddies slower than 10 cm/s and 93% slower than 20 cm/s. This range is similar to observations [*Chelton et al.*, 2011, Figure 22]. Speeds higher than

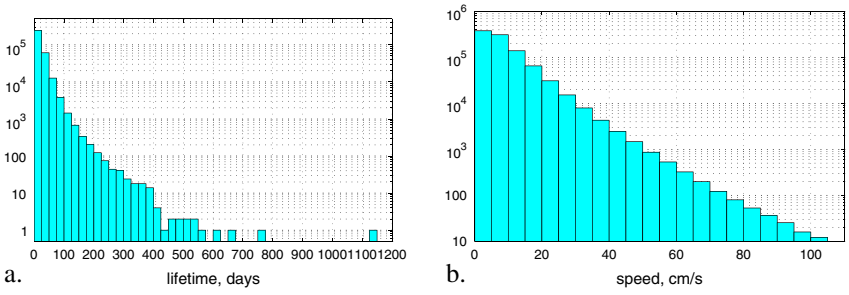

Figure 7. Distribution of eddies detected by (a) lifetime and (b) propagation speed, using the R^2 method. The majority of eddies are relatively slow and short-lived, but some eddies exist for more than a year. In Figure 7a, the vertical axis shows the eddy count for all 7 years, and each eddy is only counted once over its lifetime. In Figure 7b, the vertical axis shows the number of eddies per year counted in each daily snapshot. Eddies in Figure 7b have a minimum lifetime of 4 weeks.

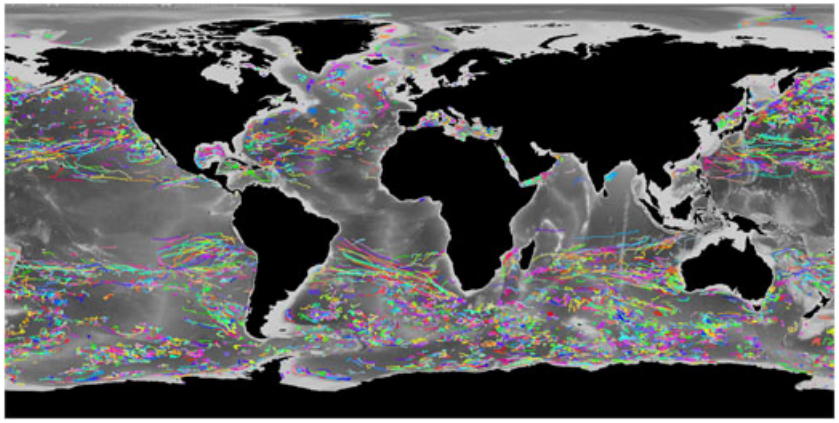

Figure 8. Tracks trace each eddy over its lifetime for the 5000 longest-lived eddies over the 7 year simulation overlayed on a grayscale bathymetry map. Colors are randomly assigned to identify each eddy track.

20 cm/s are visible in the strong currents of the Gulf Stream, Kuroshio, equatorial jets, and the ACC (Figure 4e).

[33] In order to characterize the effects of eddies over their lifetimes, the average distance, speed, and direction were computed using the locations of the first and last day provided by the tracking algorithm (Figure 9). The globe was separated into regions as follows: Southern Ocean south of 42°S; North Atlantic: 0°N–65°N and 90°W–20°E; South Atlantic: 0°S–42°S and 65°E–20°E; North Pacific: 0°N–65°N and 100°E–90°W; South Pacific: 0°S–42°S and 100°E–65°W; and Indian: 42°S–30°N and 20°E–100°E. The Southern Ocean stands out as the region with the shortest lifetime distance, with most eddies traveling less than 100 km. This can be seen qualitatively in the images of eddy

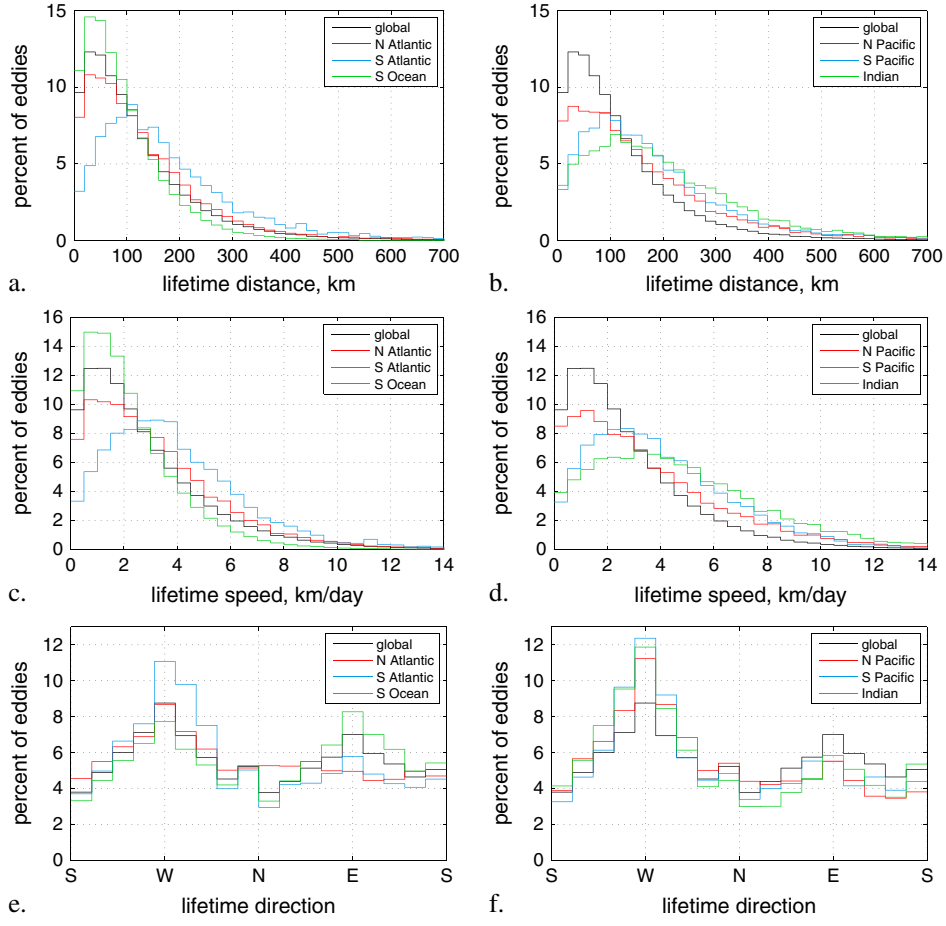

Figure 9. Statistics averaged over the lifetime of an eddy: (a, b) distance, (c, d) speed, and (e, f) direction, shown for various regions. Only eddies with a minimum lifetime of 28 days are considered.

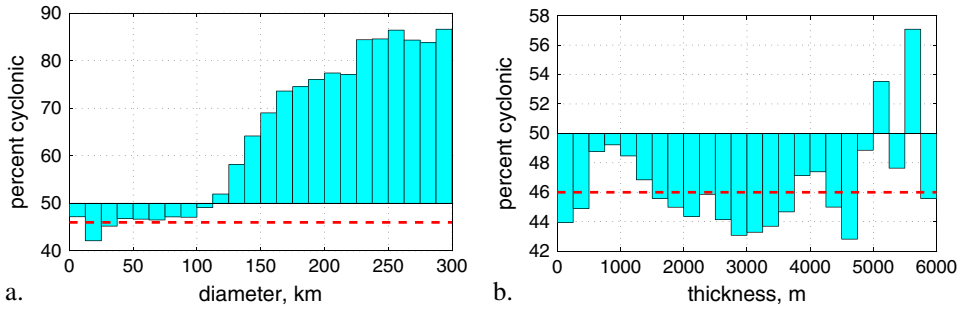

Figure 10. Percent of eddies that are cyclonic, binned by (a) diameter and (b) thickness. Overall, 46% of eddies are cyclonic (dashed line). A strong correlation exists between cyclonicity and eddy diameter, and there appears to be little dependance on thickness.

tracks (Figure 8) and is due to the pervasively strong flows of the ACC. Over most of the globe, there is a strong preference for westward motion over the lifetime of the eddy, as expected from Rossby wave dynamics. The Southern Ocean presents an exception, where the eastward background flow may be as fast or faster than the eddy's intrinsic propagation speed. Outside of the Southern Ocean, eddies in the Northern Hemisphere travel shorter distances and slower speeds than those in the Southern Hemisphere. Figure 8 shows more long, smooth paths between the equator and 42°S, while eddy tracks in the strong western boundary currents of the Northern Hemisphere are short and chaotic.

4.2. Eddy Diameter

[34] Figure 4b shows a global view of the effective diameter of the identified eddies, defined as $d = 2\sqrt{A/\pi}$, where A is the horizontal cross-sectional area of the eddy recorded at the depth with the most negative Okubo-Weiss value. Clearly the eddy diameter is a strong function of latitude, with smaller eddies near the poles and larger ones near the equator. This is expected since the first baroclinic Rossby radius varies strongly with latitude (as shown by the dashed line in Figure 6c), and length scales for mesoscale eddies typically are linearly related to the Rossby radius but are larger [*Stammer*, 1997].

[35] Zonal averages of eddy length scales provide another opportunity for quantitative comparison of the R^2 method with Okubo-Weiss, as well as with *Chelton et al.* [2011] (Figure 6c). The R^2 method removes many of the small and poorly formed eddies identified by the Okubo-Weiss method, thus increasing the average diameter, especially after filtering out relatively short-lived eddies. As with the eddy density, comparisons of length scale with data should

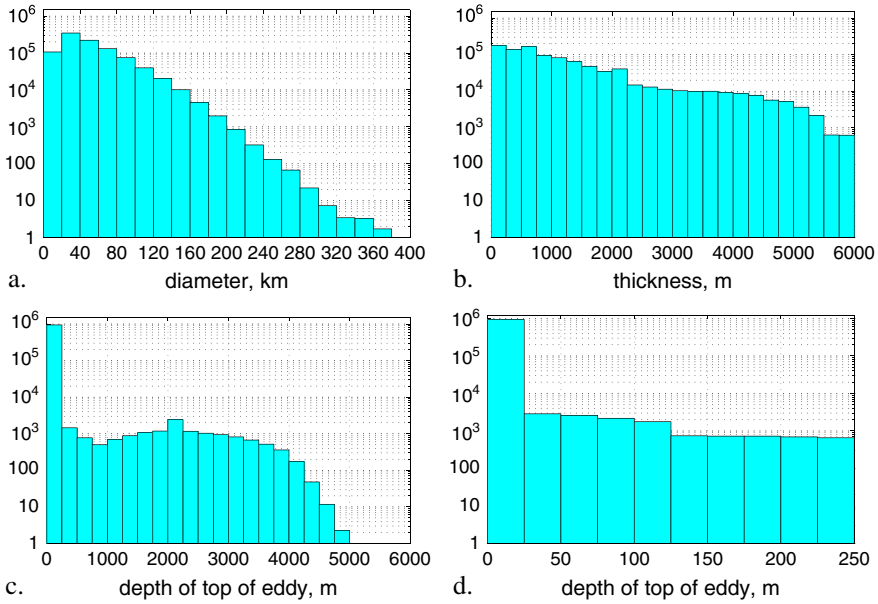

Figure 11. Distribution of eddies detected by (a) diameter, (b) thickness, and (c, d) depth of the top of the eddy, using the R^2 method and minimum lifetime of 4 weeks. The last plot (Figure 11d) shows detail of the first bar in Figure 11c. Data include the population of eddies recorded each day for 7 years, and vertical axes display the number of eddies per year. The majority of eddies are small and thin, but there are still thousands of eddies with diameters greater than 200 km and tens of thousands with thicknesses of 4000–5000 m. The great majority extend to the surface (in Figure 11c), but tens of thousands exist below the surface.

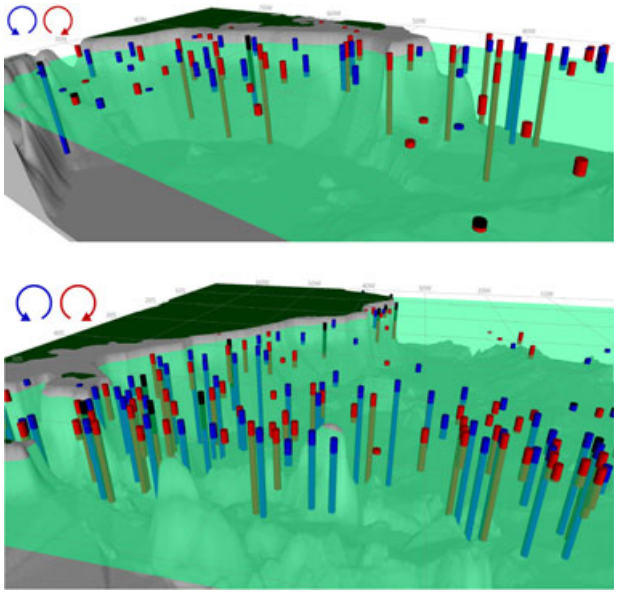

Figure 12. Skeletonized view of eddies in (a) the North Atlantic and (b) the South Atlantic. The translucent green planes are at 700 m (in Figure 12a) and 500 m (in Figure 12b). These images show the depth of penetration of the eddies; most extend to the bottom in the Antarctic Circumpolar Current region, while less than half of the Gulf Stream eddies penetrate deeply. Eddies with positive vorticity are red above the planes and yellow below; eddies with negative vorticity are blue above the planes and cyan below. Black columns extend the subsurface eddies to the surface to aid visualization. Depth is exaggerated by a factor of 50. (Image from Figures 4 and 5 of *Williams et al.* [2011a]).

focus more on shapes than magnitudes (*Chelton et al.* [2011] describe four methods of computing eddy length scales in their appendix B.3, which vary by as much as a factor of 3.7 in overall scale). The Pearson correlation coefficient (computed for latitudes where observations are available (68°S to 70°N) and outside of the tropics) relating the zonally averaged model to data length scales (black and purple curves in Figure 6c, respectively) is 0.94; a value of 1.0 is expected if the two curves are proportional or offset. Although the model and data agree very well, they both have a somewhat weaker dependence on latitude than the Rossby radius. Zonal averages of eddy diameter with varying confidence thresholds were computed using a single year's data (Figure 3c). The Pearson correlation coefficient increases systematically with increasing confidence threshold: 0.901 for 80%, 0.925 for 85%, 0.941 for 90%, and 0.943 for 95%. The improved fit of model data versus observation provides further evidence that a 90% confidence threshold is the appropriate choice for this study.

[36] Evaluating eddy diameter by region (Figure 4b), the model agrees well with the observations (*Griffa et al.* [2008, Figure 3], *Chelton et al.* [2007, Figure 3]) in the Gulf Stream and Kuroshio Current systems, as well as in the Mozambique channel, in the "Cape Cauldron" [*Boebel et al.*, 2003] to the west of the Cape of Good Hope, and along much of the Sub-Antarctic Front in the ACC. However, it appears that the simulations and R^2 method substantially underestimate the eddy diameter in the Agulhas Retroflection (particularly directly south of the African continent) and the Brazil-Malvinas Confluence. The striking maximum in the South Atlantic at about 20°S is due to a few large Agulhas eddies that have traversed the ocean quite a bit too far to the north.

4.3. Cyclonicity

[37] The direction of eddy rotation, averaged by 1° bins, is shown in Figure 4d. In the Indian ocean, a blue cyclonic band is visible between 10°S and 20°S, while a red anticyclonic band appears between 20°S and 30°S. This is similar to Lagrangian drifter survey data [*Griffa et al.*, 2008, Figure 3]. The data hint at some other coherent zonal structures, but overall spatial patterns are difficult to find, much like satellite observations [*Chelton et al.*, 2011, Figure 4].

[38] The eddy census includes more anticyclonic eddies; 46% of eddies are cyclonic overall. This behavior varies smoothly with diameter, with small (large) diameter eddies tending to be more anticyclonic (cyclonic) (Figure 10a). This behavior crosses over at 120 km in diameter, and eddies larger than 225 km in diameter have a strong preference for cyclonic behavior. Cyclonicity does not appear to vary with thickness in a regular way (Figure 10b). To our knowledge, there are no reported observations of cyclonicity as a

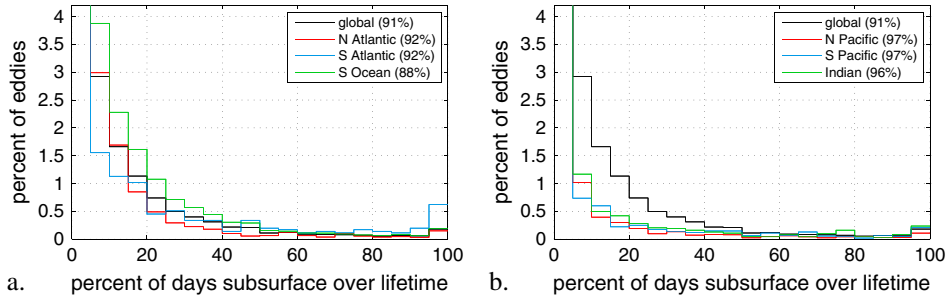

Figure 13. Distribution showing percent of days eddies are subsurface over their lifetime for various regions for eddies with lifetimes of at least 28 days. Here subsurface means the top surface of the detected eddy is below 100 m. Parenthesis on the legends show the value of the 0–5% bin so that the vertical scale can show the detail of the other categories. The values in the legend show that the great majority of eddies are subsurface for 5% of the time or less; i.e., eddies nearly always extend to the surface.

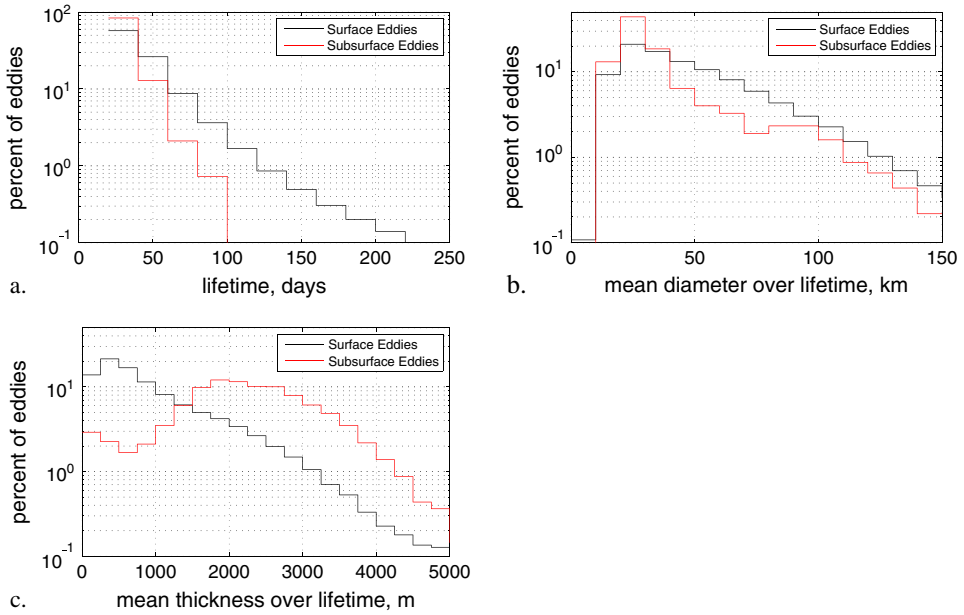

Figure 14. Characteristics of surface versus subsurface eddies for eddies with lifetimes of at least 28 days. Subsurface eddies are defined as those below 100 m at least 50% of their lifetime, and surface eddies are below 100 m 5% of their lifetime or less. Subsurface eddies have a (a) shorter lifetime and (b) smaller diameter than surface eddies. (c) Subsurface eddies have a larger percentage of eddies thicker than 1500 m than surface eddies. Overall, most eddies are thin surface eddies that only extend 500–1000 m below the surface (Figure 14c).

function of diameter or thickness. *Chelton et al.* [2011] reports more cyclones than anticyclones for eddies with a lifetime of less than 60 weeks, which is opposite our finding.

4.4. Origin and Termination

[39] The tracking algorithm allows the identification of origin and termination locations for each eddy. These were collected in 1° bins to show regions of origin and termination (not shown). The geographical distribution of origin and termination are largely the same as each other and similar to daily recorded eddy locations (Figure 4a); these are all highest in the ACC, Gulf Stream, and Kuroshio Current regions. *Chelton et al.* [2011] also find that origin and termination sites are common in open-ocean regions wherever propagating eddies occur (their Figure 6). This is consistent with studies that show that nearly all of the world ocean is baroclinically unstable [*Smith*, 2007; *Stammer*, 1998]. Plotting the difference between origin and termination global distributions (not shown), coastal regions have a higher number of eddy generation sites on eastern boundaries and more terminations on western boundaries, as one would expect when a majority of eddies are propagating westward (Figures 9e and 9f). This same pattern is evident in satellite observations [*Chelton et al.*, 2011, Figure 6]. As noted by *Dong et al.* [2012] in their regional simulations of the Southern California Bight, eddy creation can be strongly influenced by topography, which can also be seen in this global simulation.

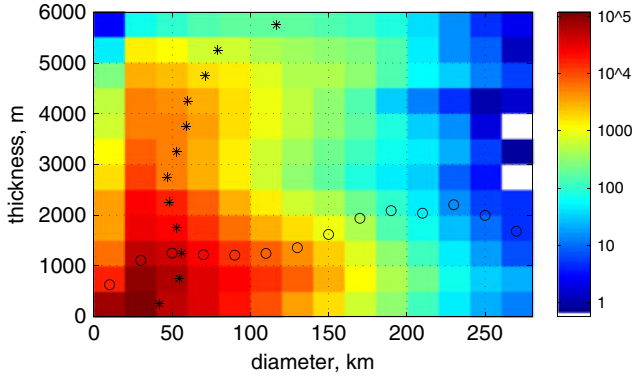

Figure 15. Distribution of eddies binned by diameter versus thickness using R^2 method and minimum lifetime of 4 weeks. Colors show a log scale of number of eddies recorded daily, per year. For each thickness category, the mean diameter is starred; for each diameter category, mean thickness is circled. A weak correlation is seen—thick eddies tend to be larger in diameter than thin eddies.

4.5. Vertical Characteristics

[40] One major advantage of using fully three-dimensional model fields is the ability to investigate the vertical characteristics of eddies. For each eddy, the R^2 method finds the highest Okubo-Weiss value where the 90% confidence threshold is maintained. The three-dimensional surface of this Okubo-Weiss value defines the eddy extent, so that the census database includes a minimum depth, maximum depth, and thus a thickness (difference between the two) for each eddy on every day. The R^2 method finds the eddy surface by determining where the Okubo-Weiss value no longer fits, to a particular confidence threshold,

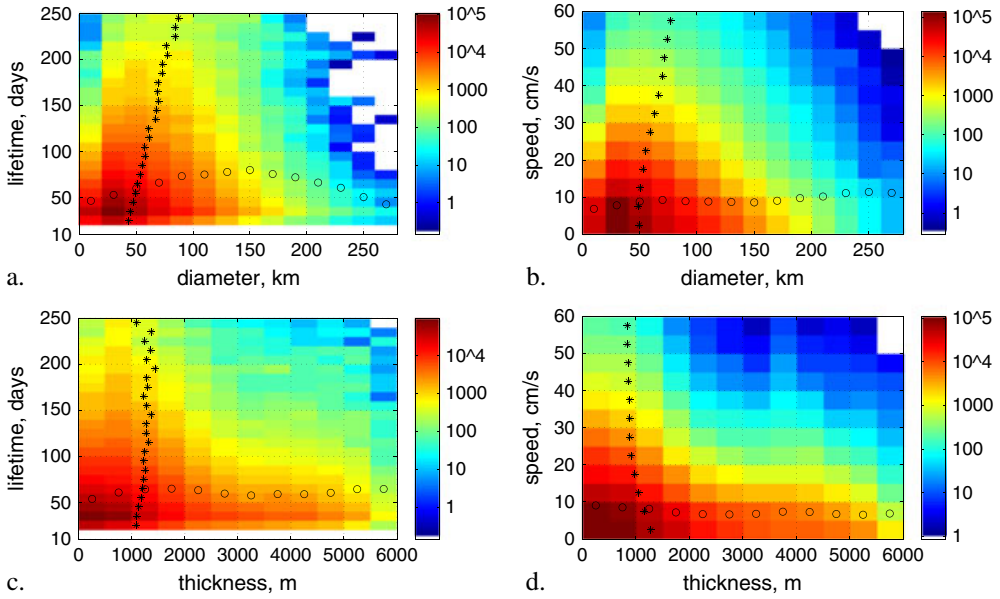

Figure 16. Distribution of eddies binned by (a, c) lifetime and (b, d) propagation speed versus (a, b) diameter and (c, d) thickness, all using R^2 method and minimum lifetime of 4 weeks. For each category, an asterisk is placed at the average of the horizontal variable, and a circle at the average of the vertical variable. White areas contain no data. Colors show a log scale of number of eddies recorded daily, per year. These trends show that longer-lived and faster eddies tend to be larger in diameter (Figures 16a and 16b), and very thin eddies are shorter-lived and faster (Figures 16c and 16d).

the linear relationship that would be expected with the inclusion of additional volume if the eddy's vorticity were perfectly Gaussian in its dependence on radial distance from the core. There will be some vortical motion beyond the eddy's boundary surface, but it is substantially weaker than within the eddy.

[41] The zonally binned thickness (Figure 6b) is the greatest in the Southern Ocean, due in part to a fairly uniform longitudinal distribution in the ACC as well as some very thick eddies to the north and west of the Weddell Sea (Figure 4c). Thick eddies (∼2000 m) are also typically found in the extension regions of the major western boundary currents as well as the North Brazil Current and the Gulf of Mexico.

[42] As is the case for the horizontal scale, the R^2 method does not have an explicit thickness criteria, but thin eddies are more strongly removed than with Okubo-Weiss alone because most poorly formed eddies are also thin. The R^2 method approximately doubles the globally averaged thickness, compared to Okubo-Weiss, and restricting to eddies with a minimum lifetime of 4 weeks further removes thin eddies (Figure 6b).

[43] Overall, the majority of eddies are thin (Figure 11b). Still, there is a significant population of thick eddies since the distribution shows that 40%, 16%, and 7.7% are at least 1000 m, 2000 m, and 3000 m thick, respectively. In order to provide a qualitative image of vertical eddy extent, a skeletonized view is provided in Figure 12, showing that some eddies extend to the full column depth in the Gulf Stream, while most eddies extend to the bottom in the Southern Ocean.

[44] In addition to thickness, we can also locate the extents of eddies within the water column. The great majority of eddies observed in the daily data extend all the way to the surface (Figures 11c and 11d), with 97% expressed in the model's 10 m-thick uppermost threshold for eddies tracked for at least 4 weeks and 89% with no lifetime restriction. This does not necessarily imply that the remaining eddies would be missed in observational studies of SSH using satellite altimetry. Not all eddies that extend to the surface have a clear SSH signature, while some eddies that do not reach the surface *can* be detected in the SSH. To quantify the percentage of eddies that are missed would require correlating these results with an SSH-based detection algorithm, such as *Chelton et al.* [2011], which is beyond the scope of this paper.

[45] The tracking program allows us to quantify vertical characteristics over the lifetime of each eddy. To this end, we define "subsurface" to mean that the top of the eddy boundary surface is below 100 m. Figure 13 shows the percentage of days that the eddy is subsurface over its lifetime. The great majority of eddies extend above 100 m at least 95% of the time (91% globally). One might expect that subsurface eddies remain so for the duration of their lifetime. However, that is not the case. Eddies tracked over their lifetime that are subsurface some days extend to the surface on other days. Figure 13 shows that many eddies are subsurface 5–20% of the time, and very few are subsurface all the time.

[46] Going one step further, what are the characteristics of subsurface eddies that will largely be missed by satellite observations? For this purpose, we define subsurface eddies as those below 100 m at least 50% of their lifetime and surface eddies as those below 100 m for 5% of their lifetime or less. Subsurface eddies have a much shorter lifespan than surface eddies, and no subsurface eddies were found with lifetimes longer than 125 days, while surface eddies

often live for 200–600 days (Figure 14). Subsurface eddies are smaller than surface eddies, with 40% in the 30–40 km diameter category. The thickness distribution does not follow this pattern. Most subsurface eddies are 1500–3500 m thick, while more than half of surface eddies are less than 1000 m thick.

4.6. Multivariate Distributions

[47] Given the numerous properties that the eddy census provides, it is now possible to look for relationships between them. For example, Figure 15 shows a two-dimensional histogram of diameter and thickness. For most of the range of both diameter (50–150 m) and thickness (500–4500 m), there is no clear correlation. That is, knowledge of an eddy's diameter yields no specific information about its thickness, and vice versa. However, the extremes in the distribution do show that small eddies tend to be thinner than normal and very thick eddies tend to have larger diameters than normal. Quantitatively, the Pearson correlation coefficient between diameter and thickness is 0.154, where 1.0 means the two variables are linearly dependent, and zero implies no correlation.

[48] Based on kinematic considerations, one might expect that larger eddies would tend to be longer lived than smaller ones since they contain more mass and momentum and are less likely to be torn apart by background shear or when passing over deep-sea ridges. This does appear to be the case here. A clear correlation exists between mean eddy diameter and lifetime (stars in Figure 16a), as quantified by a Pearson correlation coefficient of 0.261. Similarly, fast eddies tend to be larger in diameter (stars in Figure 16b). There also is a noticeable relationship between thickness and speed, showing a tendency for thinner eddies to move somewhat faster. Quantitatively, however, the Pearson correlation is only 0.017 so this may only be relevant to speeds under about 20 cm/s.

5. Conclusions

[49] Seven years of daily output from a global high-resolution POP simulation has allowed us to locate and characterize 6.7 million eddies using the R^2 method [*Williams et al.*, 2011b] and a tracking algorithm. While this work is preceded by many studies of eddies in regional ocean simulations such as *Doglioli et al.* [2007], *Nencioli et al.* [2010], *Souza et al.* [2011b], *Dong et al.* [2012], *Doglioli et al.* [2007], and *Colas et al.* [2011] (a few of which also evaluate the vertical aspects of the eddy field), we believe that this is the first systematic eddy census of a three-dimensional high-resolution global ocean simulation. Our goal in this study is to provide statistical information on eddies throughout the global ocean, as done with satellite altimetry investigations [*Chelton et al.*, 2007; *Chelton et al.*, 2011], and to also describe eddy characteristics that are hidden below the surface. In addition, detailed quantitative information about eddy speed and lifetime may prove useful in attempts to parameterize the nonlocal effects of eddies in simulations where they are not explicitly represented.

[50] A significant number of eddies penetrate deep into the ocean: a third of the eddies in this simulation are at least 1000 m tall. Of eddies with a minimum 4 weeks lifetime, the majority (97%) extend all of the way to the surface. Although not all of these surface-expressed eddies located by the R^2 method are clearly reflected in the surface height, it is very likely that satellite altimetry-based assessments of eddy size, spatial distribution, and lifetime are reasonably comprehensive as estimates of eddy characteristics. The remaining eddies that do not reach the surface are distributed over the full depth of the ocean, with thousands deeper than 3000 m. Larger-diameter eddies are likely to be thicker, longer lived, and faster than smaller-diameter eddies. Correlations between thickness and lifetime or thickness and speed are weak, except that very thin eddies are fast and shorter lived.

[51] Any eddy census method is dependent on the eddy detection method and the parameters chosen within that method. Because the R^2 method is relatively new, we include a traditional Okubo-Weiss method in some plots for direct comparison. The R^2 method judges the quality of an eddy based on the similarity of certain functional fits with an idealized Gaussian vortex. We find that R^2 is more selective than Okubo-Weiss and preferentially removes smaller and thinner eddies. It improves global statistics, such as mean diameter versus latitude, to be more like observations and theoretical expectations. For this study, we have primarily used an R^2 confidence threshold of 90%, which appears to mostly select well-formed, coherent, and long-lived eddies. Absolute numbers of eddies counted are sensitive to choices of methods and parameters used for detection, so we have included distributions and percentages throughout the paper. Choices of model settings, such as diffusion coefficients and advection schemes, can also affect the number and characteristics of simulated eddies, but quantifying sensitivity to these factors is prohibitively expensive for a global eddying model. In addition, experience has shown that there is a relatively narrow range of parameter space that provides smooth solutions and yet allows for strongly developed mesoscale variability that compares well with observations [*Bryan et al*., 2007]. Thus, it is unlikely that acceptable variations in the model configuration would result in substantial changes to the results presented here.

[52] The first priority in an ocean modeling study is to confirm that simulations are in reasonable agreement with observational data, wherever those data are available. Other authors have conducted comparisons of the POP ocean model at a resolution of one-tenth degree with observations of volume transport, kinetic energy, and eddy kinetic energy and have found good agreement [*Smith et al.*, 2000; *Bryan et al.*, 2007; *Maltrud and McClean*, 2005]. In the eddy data presented here, a comparison of eddy count, diameter, and rotational direction was made with figures in *Chelton et al.* [2011] and *Griffa et al.* [2008]. General trends, such as increasing diameter towards the equator, are similar to observed, but geographical distributions of eddy characteristics did not match in some cases. This was complicated by the fact that satellite observations [*Chelton et al.*, 2011] and drifter trajectories [*Griffa et al.*, 2008] were not always in agreement.

[53] Beyond surface studies, is there a way to confirm the deeper data? Here we turn to *Thoppil et al.* [2011], who found that a simulation using the Hybrid Coordinate Ocean Model (HYCOM) at 1/12.5° resolution is deficient in eddy kinetic energy in both the upper and abyssal oceans (depths greater than 3000 m) by 21% and 24%,

respectively, compared to surface drifting buoys and deep current meters (increasing the resolution to 1/25° alleviated the problem). Our study used a 1/10° POP simulation, but generally we can expect that ocean simulations at this resolution may be underresolved for some eddy processes and may underrepresent eddy activity, perhaps by as much as 20–25%.

[54] Even with this discrepancy, we can confidently conclude that eddies are a common phenomenon in the deep ocean, albeit in smaller numbers than thin eddies near the surface. Observational studies of eddy transport of heat and nutrients [*Roemmich and Gilson*, 2001; *Chaigneau et al.*, 2011; *Doglioli et al.*, 2007] have been confined to the upper ocean for practical reasons. The next step in the analysis of this simulation is to quantify the impact of discrete eddies on the transport of tracers throughout the globe. Indeed, high-resolution ocean model output provides the unique opportunity to compute detailed statistics where observations are sparse. Our team has recently developed a method to compute tracer fluxes through eddy boundaries [*Williams et al.*, 2012]. In future work, we plan to seed eddies in global simulations with passive tracers, leading to eddy transport and containment statistics for various regions of the earth.

[55] **Acknowledgments.** The authors thank Milena Veneziani and Wilbert Weijer for early comments on the manuscript and Neesha Regmi Schnepf for assistance with the literature search on vortex identification methods. We also thank Richard Strelitz and Samantha Oestricher for insightful discussions. Dudley Chelton and Michael Schlax generously gave us access to their altimetry-derived eddy census data. M.R.P., M.W.H., and M.E.M. were supported by the Regional and Global Climate Modeling programs; S.J.W. was supported by the UV-CDAT project in the Climate and Earth System Modeling programs. Both of these are within the Office of Biological and Environmental Research of the US Department of Energy's Office of Science. We acknowledge the support of the LANL-UC Davis Materials Design Institute for S.J.W. and B.H.

References

Adams, D. K., D. J. McGillicuddy, L. Zamudio, A. M. Thurnherr, X. Liang, O. Rouxel, C. R. German, and L. S. Mullineaux (2011), Surface-generated mesoscale eddies transport deep-sea products from hydrothermal vents, *Science*, *332*, 580–583.

Adcroft, A., C. Hill, and J. Marshall (1997), Representation of topography by shaved cells in a height coordinate ocean model, *Mon. Weather Rev.*, *125*, 2293.

Benitez-Nelson, C. R., et al. (2007), Mesoscale Eddies drive increased silica export in the subtropical Pacific ocean, *Science*, *316*, 1017–1021.

Boebel, O., J. Lutjeharms, C. Schmid, W. Zenk, T. Rossby, and C. Barron (2003), The Cape Cauldron: A regime of turbulent inter-ocean exchange, *Deep-Sea Res. Pt. II*, *50*, 57–86.

Bryan, F. O., M. W. Hecht, and R. D. Smith (2007), Resolution convergence and sensitivity studies with North Atlantic circulation models. Part I: The Western Boundary Current system, *Ocean Model.*, *16*, 141–159.

Chaigneau, A., and O. Pizarro (2005), Eddy characteristics in the eastern South Pacific, *J. Geophys. Res.-Oceans*, *110*, 6005, doi: 10.1029/2004JC002815.

Chaigneau, A., M. Le Texier, G. Eldin, C. Grados, and O. Pizarro (2011), Vertical structure of mesoscale eddies in the eastern South Pacific Ocean: A composite analysis from altimetry and Argo profiling floats , *J. Geophys. Res.-Oceans*, *116*, 11,025, doi:10.1029/2011JC007134.

Chelton, D. B., M. G. Schlax, R. M. Samelson, and R. A. de Szoeke (2007), Global observations of large oceanic eddies, *Geophys. Res. Lett.*, *34*, 5, doi:10.1029/2007GL030812.

Chelton, D. B., M. G. Schlax, and R. M. Samelson (2011), Global observations of nonlinear mesoscale eddies, *Prog. Oceanogr.*, *91*, 167–216.

Colas, F., J. C. McWilliams, X. Capet, and J. Kurian (2011), Heat balance and eddies in the Peru-Chile current system, *Clim. Dynam.*, *39*(1-2), 582.

Dewar, W. K., and P. D. Killworth (1995), On the stability of oceanic rings, *J. Phys. Oceanogr.*, *25*, 1467–1487.

Doglioli, A. M., B. Blanke, S. Speich, and G. Lapeyre (2007), Tracking coherent structures in a regional ocean model with wavelet analysis: Application to Cape Basin eddies, *J. Geophys. Res.-Oceans*, *112*, 5043, doi:10.1029/2006JC003952.

Dong, C., X. Lin, Y. Liu, F. Nencioli, Y. Chao, Y. Guan, D. Chen, T. Dickey, and J. C. McWilliams (2012), Three-dimensional oceanic eddy analysis in the Southern California Bight from a numerical product, *J. Geophys. Res.-Oceans*, *117*(C7), 2156–2202, doi:10.1029/2011JC007354.

Dukowicz, J. K., and R. D. Smith (1994), Implicit free-surface method for the Bryan-Cox-Semtner ocean model, *J. Geophys. Res.*, *99*, 7991–8014.

Everett, J. D., M. E. Baird, and I. M. Suthers (2011), Three-dimensional structure of a swarm of the salp Thalia democratica within a cold-core eddy off southeast Australia, *J. Geophys. Res.-Oceans*, *116*, 12,046.X, doi:10.1029/2011JC007310.

Falkowski, P. G., D. Ziemann, Z. Kolber, and P. K. Bienfang (1991), Role of eddy pumping in enhancing primary production in the ocean, *Nature*, *352*, 55–58.

Fang, F., and R. Morrow (2003), Evolution, movement and decay of warm-core Leeuwin Current eddies, *Deep-Sea Res. Pt. II*, *50*, 2245–2261.

Godø, O. R., A. Samuelsen, G. J. Macaulay, R. Patel, S. S. Hjøllo, J. Horne, S. Kaartvedt, and J. A. Johannessen (2012), Mesoscale eddies are oases for higher trophic marine life, *PLoS ONE*, *7*, e30,161.

Griffa, A., R. Lumpkin, and M. Veneziani (2008), Cyclonic and anticyclonic motion in the upper ocean, *Geophys. Res. Lett.*, *35*, 1608, doi: 10.1029/2007GL032100.

Griffies, S.M., et al. (2009), Coordinated Ocean-Ice Reference Experiments (COREs), *Ocean Model.*, *26*, 1–46.

Henson, S. A., and A. C. Thomas (2008), A census of oceanic anticyclonic eddies in the Gulf of Alaska, *Deep-Sea Res. Pt. I*, *55*, 163–176.

IPCC (2007), *Climate Change 2007: The Physical Science Basis. Contribution of Working Group I to the Fourth Assessment Report of the Intergovernmental Panel on Climate Change*, 996 pp., Cambridge University Press, Cambridge U. K.

Isern-Fontanet, J., E. Garca-Ladona, and J. Font (2003), Identification of marine eddies from altimetric maps, *J. Atmos. Ocean. Tech.*, *20*, 772.

Isern-Fontanet, J., E. Garca-Ladona, J. Font, and A. Garca-Olivares (2006), Non-Gaussian velocity probability density functions: An altimetric perspective of the mediterranean sea, *J. Phys. Oceanogr.*, *36*, 2153–2164.

Kundu, P. K., I. M. Cohen, and D. R. Dowling (2012), *Fluid Mechanics,* 5th ed., 920 pp., Academic Press, New York, N. Y.

Large, W. G., J. C. McWilliams, and S. C. Doney (1994), Oceanic vertical mixing: A review and a model with a nonlocal boundary layer parameterization, *Rev. Geophys.*, *32*, 363–404.

de Leeuw, W. C., and F. H. Post (1994), A statistical view on vector fields, in *Visualization in Scientific Computing*, edited by M. Göbel, H. Müller, and B. Urban, pp. 53–62, Springer-Verlag Wein.

Lilly, J. M., and P. B. Rhines (2002), Coherent eddies in the labrador sea observed from a mooring, *J. Phys. Oceanogr.*, *32*, 585–598.

Mahadevan, A., E. D'Asaro, C. Lee, and M. J. Perry (2012), Eddy-driven stratification initiates north atlantic spring phytoplankton blooms, *Science*, *337*, 54–58.

Maltrud, M., F. Bryan, and S. Peacock (2010), Boundary impulse response functions in a century-long eddying global ocean simulation, *Environ. Fluid. Mech.*, *10*, 275–295, doi:10.1007/s10652-009-9154-3.

Maltrud, M. E., and J. L. McClean (2005), An eddy resolving global 1/10° ocean simulation, *Ocean Model.*, *8*, 31–54.

Maslowski, W., J. L. C. Kinney, D. C. Marble, and J. Jakacki (2008), Towards eddy-resolving models of the Arctic ocean, in *Ocean Modeling in an Eddying Regime*, edited by M. Hecht, and H. Hasumi, pp. 241–264, no. 177 in Geophysical Monograph Series, American Geophysical Union, Washington, D.C.

Meehl, G. A., et al. (2006), Climate change projections for the twenty-first century and climate change commitment in the CCSM3, *J. Climate*, *19*, 2597–2616.

Nencioli, F., C. Dong, T. Dickey, L. Washburn, and J. C. McWilliams (2010), A vector geometry-based eddy detection algorithm and its application to a high-resolution numerical model product and high-frequency radar surface velocities in the Southern California Bight, *J. Atmos. Ocean. Tech.*, *27*, 564–579.

Nishino, S., M. Itoh, Y. Kawaguchi, T. Kikuchi, and M. Aoyama (2011), Impact of an unusually large warm-core eddy on distributions of nutrients and phytoplankton in the southwestern Canada Basin during late summer/early fall 2010 , *Geophys. Res. Lett.*, *38*(16), 602, doi: 10.1029/2011GL047885.

Paillet, J., C. Le B., X. Carton, Y. Morel, and A. Serpette (2002), Dynamics and evolution of a Northern Meddy, *J. Phys. Oceanogr.*, *32*, 55–79.

Petersen, M. R., K. Julien, and J. B. Weiss (2006), Vortex cores, strain cells, and filaments in quasigeostrophic turbulence, *Phys. Fluids*, *18*, 026601, 11 pp., doi:10.1063/1.2166452.

Prater, M. D. (2002), Eddies in the Labrador Sea as observed by profiling RAFOS floats and remote sensing, *J. Phys. Oceanogr.*, *32*, 411–427.

Riser, S. C., W. B. Owens, H. T. Rossby, and C. C. Ebbesmeyer (1986), The structure, dynamics, and origin of a small-scale lens of water in the Western North Atlantic thermocline, *J. Phys. Oceanogr.*, *16*, 572–590.

Roemmich, D., and J. Gilson (2001), Eddy transport of heat and thermocline waters in the North Pacific: A key to interannual/decadal climate variability? *J. Phys. Oceanogr.*, *31*, 675–688.

Sadarjoen, I. A., and F. H. Post (2000), Detection, quantification, and tracking of vortices using streamline geometry, *Comput. Graph.*, *24*, 333–341.

Shoosmith, D. R., P. L. Richardson, A. S. Bower, and H. T. Rossby (2005), Discrete eddies in the northern North Atlantic as observed by looping RAFOS floats, *Deep-Sea Res. Pt. II*, *52*, 627–650.

Smith, K. S (2007), The geography of linear baroclinic instability in Earth's oceans, *J. Mar. Res.*, *65*, 655–683.

Smith, R. D., J. K. Dukowicz, and R. C. Malone (1992), Parallel ocean general circulation modeling, *Physica D*, *60*, 38–61.

Smith, R. D., M. E. Maltrud, F. O. Bryan, and M. W. Hecht (2000), Numerical simulation of the North Atlantic Ocean at 1/10°, *J. Phys. Oceanogr.*, *30*, 1532–1561.

Souza, J. M. A. C., C. de Boyer Montégut, C. Cabanes, and P. Klein (2011a), Estimation of the Agulhas ring impacts on meridional heat fluxes and transport using ARGO floats and satellite data, *Geophys. Res. Lett.*, *38*(21), 602, doi:10.1029/2011GL049359.

Souza, J. M. A. C., C. de Boyer Montégut, and P. Y. Le Traon (2011b), Comparison between three implementations of automatic identification algorithms for the quantification and characterization of mesoscale eddies in the South Atlantic Ocean, *Ocean Sci.*, *7*, 317–334.

Stammer, D. (1997), Global characteristics of ocean variability estimated from regional TOPEX/POSEIDON Altimeter measurements, *J. Phys. Oceanogr.*, *27*, 1743–1769.

Stammer, D (1998), On eddy characteristics, eddy transports, and mean flow properties, *J. Phys. Oceanogr.*, *28*, 727–739.

Thoppil, P. G., J. G. Richman, and P. J. Hogan (2011), Energetics of a global ocean circulation model compared to observations, *Geophys. Res. Lett.*, *38*(15), 607, doi:10.1029/2011GL048347.

Timmermans, M.-L., J. Toole, A. Proshutinsky, R. Krishfield, and A. Plueddemann, (2008), Eddies in the Canada basin, arctic ocean, observed from ice-tethered profilers, *J. Phys. Oceanogr.*, *38*, 133.

Williams, S., M. Hecht, M. Petersen, R. Strelitz, M. Maltrud, J. Ahrens, M. Hlawitschka, and B. Hamann (2011a), Visualization and analysis of eddies in a global ocean simulation, *Comput. Graph. Forum*, *30*, 991–1000.

Williams, S., M. Petersen, P.-T. Bremer, M. Hecht, V. Pascucci, J. Ahrens, M. Hlawitschka, and B. Hamann (2011b), Adaptive extraction and quantification of geophysical vortices, *IEEE T. Vis. Comput. Gr.*, *17*, 2088–2095.

Williams, S., M. Petersen, M. Hecht, M. Maltrud, J. Patchett, J. Ahrens, and B. Hamann (2012), Interface exchange as an indicator for eddy heat transport, *Comput. Graph. Forum*, *31*, 1125–1134.

Williams, S. J. (2012), Identification and quantification of mesoscale eddies in a global ocean simulation, Ph.D. thesis, University of California, Davis.

Xiu, P., F. Chai, L. Shi, H. Xue, and Y. Chao (2010), A census of eddy activities in the South China Sea during 1993-2007, *J. Geophys. Res.*, *115*, 564–579, doi:10.1029/2009JC005657.